RESEARCH ARTICLE OPEN ACCESS

Tape-Cast NMC-LLZO-LBO-based Composite Cathodes for Solid-State Lithium Batteries

Kaouther Touidjine[1,2,5] | Christoph Roitzheim[1] | Xiaochen Liu[1] | Walter Sebastian Scheld[1] | Andreas Paulus[1] | Muhammad Zubair[1] | Mark Huijben[3] | Erik Kelder[2] | Marnix Wagemaker[2] | Martin Finsterbusch[1,4] | Dina Fattakhova-Rohlfing[1,4,5]

[1]Institute of Energy Materials and Devices: Materials Synthesis and Processing (IMD-2), Forschungszentrum Jülich GmbH, Jülich, Germany | [2]Faculty of Applied Sciences, Department of Radiation Science and Technology, Delft University of Technology, The Netherlands | [3]MESA+ Institute for Nanotechnology, University of Twente, The Netherlands | [4]Helmholtz Institute Münster: Ionics in Energy Storage (IMD-4), Forschungszentrum Jülich GmbH, Münster, Germany | [5]Faculty of Engineering and Center for Nanointegration Duisburg-Essen (CENIDE), University of Duisburg-Essen, Duisburg, Germany

Correspondence: Dina Fattakhova-Rohlfing (d.fattakhova@fz-juelich.de)

Received: 31 December 2025 | **Revised:** 14 April 2026 | **Accepted:** 14 April 2026

Keywords: electronic percolation | LLZO all-solid-state batteries | NMC composite cathodes | tape casting

ABSTRACT

In order to increase the industrial appeal of solid-state batteries (SSBs) based on garnet $Li_7La_3Zr_2O_{12}$ (LLZO), the possibility of manufacturing them using scalable production processes such as tape casting must be demonstrated. In particular, the scalable production of thick, high-capacity oxide-ceramic composite cathodes based on Ni-rich $LiNi_xMn_yCo_zO_2$ (NMC) remains a key challenge on the path to realizing ceramic SSBs with competitive energy densities. The limited thermal compatibility between NMC and LLZO during sintering requires the use of a sintering aid such as Li_3BO_3 (LBO), which, however, impairs the rheological stability of tape casting slurries. In this work, we have developed a new tape-casting process for thick oxide-ceramic composite cathodes by establishing a slurry formulation that is compatible with multiphase cathode compositions and enables the reproducible fabrication of composite NMC cathode tapes with high active material loading. Two cathode configurations are investigated: NMC-LLZO-LBO composite cathodes, where LLZO serves as the catholyte, and LLZO-free NMC-LBO cathodes. After cosintering, the residual porosity of the ceramic cathodes is infiltrated with a polymer electrolyte with and without conductive carbon additives to form hybrid polymer-ceramic SSBs. By systematically correlating cathode chemistry, secondary phase formation, and electrochemical performance, this study demonstrates how cathode chemistry and the balance between ionic and electronic transport pathways influence capacity utilization and cycle stability in thick, tape-cast NMC-based composite cathodes.

1 | Introduction

Solid-state batteries (SSBs), which use a solid-state electrolyte (SSE) instead of a liquid one, are considered as a promising technology that can overcome many of the challenges of current Li-ion batteries (LIBs), including energy density and safety [1, 2]. In particular, oxide ceramic cells based on the garnet-type SSE $Li_7La_3Zr_2O_{12}$ (LLZO) have received continuous attention since LLZO has a wide electrochemical stability window (0–6 V vs. Li/Li^+) [3], low electronic conductivity of 10^{-8} S cm^{-1} [4], moderately high lithium-ion conductivity of up to $2{\cdot}10^{-3}$ S cm^{-1} at room temperature [5], and remarkable chemical stability, which allows its synthesis and processing under ambient conditions [6, 7]. In addition, the high reduction stability of Ta-substituted LLZO ($Li_{6.45}Al_{0.05}La_3Zr_{1.6}Ta_{0.4}O_{12}$, LLZO:Ta) enables the use of Li-metal anodes, allowing garnet-type SSBs to achieve higher energy density than conventional LIBs with graphite anodes

while offering high intrinsic safety due to the nonflammability of LLZO [8–11].

The realization of oxide-based SSBs with high capacity and competitive energy density depends crucially on the design of thick composite cathodes with high active material loading. However, in ceramic solid-state systems, a fundamental complication arises due to the solid and rigid nature of LLZO, which cannot infiltrate the cathode layer to wet the cathode active material (CAM) particles and form spontaneously ionically conductive interfaces, as is the case in conventional LIBs with liquid electrolytes. Consequently, a three-dimensional composite cathode architecture is required in which the CAM is combined with a solid-state ionic conductor ('catholyte'), typically LLZO itself. Therefore, the CAM and LLZO must be sintered together at elevated temperatures to establish good interfacial contact between CAM and catholyte particles and to ensure a three-dimensional percolation network of ion and electron conduction pathways across the entire cathode thickness [12–14]. The formation of an optimized, intertwined composite cathode morphology with low interfacial resistance is critical for high conductivity of the cathode layer and effective utilization of the CAM [15–17], but becomes increasingly difficult with increasing layer thickness and CAM loading.

Since LLZO (and SSEs generally) have a higher relative density than liquid electrolytes, high-voltage, high-capacity CAMs are required to achieve competitive energy density in composite cathode morphologies. For these reasons, Ni-rich $LiNi_xMn_yCo_zO_2$ (NMC) are particularly attractive CAMs for SSBs [18]. However, integrating NMC into LLZO-based composite cathodes poses a fundamental challenge during cosintering. While effective densification of LLZO typically requires temperatures above 1000°C [19, 20], NMC exhibits thermal incompatibility with LLZO already at temperatures above 600°C [14, 21, 22]. Under these conditions, diffusion-driven reactions are activated, leading to chemical decomposition and the formation of secondary phases that impair electrochemical functionality [15–17]. The thermal compatibility between NMC and LLZO, including the amount and nature of the formed side phase, as well as the reaction onset temperature, depends strongly on the NMC composition. The low-capacity, Mn-rich NMC compositions such as $LiNi_{1/3}Mn_{1/3}Co_{1/3}O_2$ (NMC111) generally have a higher reaction onset temperature for secondary phase formation during cosintering than high-capacity, Ni-rich compositions such as $LiNi_{0.8}Mn_{0.1}Co_{0.1}O_2$ (NMC811) [14, 21]. However, although NMC811 reacts already at lower temperatures, only a small amount of one secondary phase forms as isolated particles. Therefore, the high-capacity, Ni-rich NMC compositions are also suitable CAMs for LLZO-based composite cathodes fabricated by cosintering [14]. To overcome the limited thermal compatibility between NMC and LLZO, liquid-phase sintering strategies using additives with low melting points were investigated. In particular, Li_3BO_3 (LBO) was used as a sintering aid to enable the consolidation of NMC-LLZO composite cathode at reduced temperatures of 750°C [23–25]. Using this approach, fully inorganic NMC-based SSBs were successfully fabricated by screen printing thin composite cathode layers onto dense LLZO substrates and then sintering them at low temperatures [14, 26, 27]. Although this approach allows sufficient densification of cathode layers, chemical interactions between NMC and LLZO cannot be completely suppressed [14, 28]. Compatibility studies have shown that cosintering NMC811 with LLZO above 600°C mainly leads to the formation of $La_2(Li,Ni)_{0.5}O_4$ as a side phase with low weight fractions [14, 21]. As a consequence, although the resulting cells are electrochemically active, they exhibit limited capacity utilization, with reported discharge capacities for Ni-rich NMC811-LLZO composite cathodes not exceeding 120 $mAhg^{-1}$ [14], which is well below the theoretical capacity. An alternative strategy for eliminating thermal incompatibility issues is to completely exclude LLZO from the cathode and use LBO as a catholyte. In the NMC-LBO configuration, LBO enables low-temperature sintering, serves as the Li-ion conductor, and suppresses the LLZO-related secondary phase formation. However, it should be taken into account that LBO has significantly lower (by almost three orders of magnitude) ionic conductivity compared to LLZO and is therefore generally applicable only to thin cathode layers [24]. Using screen-printing techniques, the NMC111-LBO composite cathodes have delivered a discharge capacity of up to 140 mAh g^{-1} without detectable secondary phase formation after cosintering [29]. It is noteworthy that the reported performance of LLZO-free cathodes has only been demonstrated for thin layers. When extended to thick cathodes with high CAM loading, it remains unclear whether these composite cathode configurations can be implemented successfully. It can be expected that in an LLZO-free configuration, the low ionic conductivity of LBO would lead to pronounced polarization in thicker layers, while in the LLZO-containing cathodes, the formation of detrimental secondary phases can increase the interfacial resistance and most likely further impede the ion and electron transport across the electrode thickness.

To manufacture thick ceramic NMC-based composite cathodes on an industrial scale, scalable fabrication techniques must be developed. Compared to screen printing that is mainly applicable for thin layers, tape casting enables the scalable production of free-standing ceramic layers with variable thickness and is a process of choice for the fabrication of thick composite cathode layers within this work. In a tape casting process, ceramic powder is dispersed in a mixture of solvent, dispersant, and plasticizer to form a slurry that is cast into free-standing layers with precisely controlled thickness and 3D microstructure [30]. Tape casting has already been successfully applied to produce LLZO-based composite cathodes containing $LiCoO_2$ (LCO) as a CAM [13, 31], but the fabrication of tape-cast composite ceramic cathodes with NMC has not been reported yet, mainly due to the challenges with NMC processing and sintering. In addition to lower temperature stability of NMC compared to LCO during sintering with solid electrolytes, NMC is much more prone to protonation in ambient atmosphere and in protic solvents, which interferes with solvent-binder system required for slurry fabrication and promotes gelation [30, 32, 33]. Incorporation of LBO in the slurry as sintering aid for the NMC-based composite cathodes, as discussed above adds another layer of complexity, as LBO is highly hydrophilic so that chemical stability in the slurry must be carefully controlled.

In this work, we have developed a tape-casting route to produce oxide ceramic Ni-rich NMC-based composite cathodes for SSBs. We developed a slurry formulation that enables stable dispersion of NMC, LLZO, and LBO and allows the reproducible fabrication of free-standing cathode tapes with controlled thickness and high active material loading. Two cathode configurations were investigated: (i) NMC-LLZO-LBO composite cathodes, in which LLZO with high ionic conductivity acts as catholyte and LBO serves as

the sintering aid and (ii) LLZO-free NMC-LBO cathodes, in which LBO, with its significantly lower ionic conductivity, is the only ionic conductor and thus performs both the function of a sintering aid and that of a catholyte. After cosintering, the residual porosity of the ceramic cathode tapes was infiltrated with a polymer electrolyte with and without conductive carbon additives to form hybrid polymer-ceramic SSBs. By systematically comparing the structural and chemical properties of the resulting NMC cathode configurations with their electrochemical performance in full cells with and without carbon, we elucidate how the cathode chemistry, the secondary phase formation, and the balance between ionic and electronic transport pathways govern the capacity utilization and cycling stability of tape cast Ni-rich NMC-based composite cathodes.

2 | Results and Discussion

To produce free-standing NMC-based composite cathode tapes, we adapted the established tape casting process that was developed in our previous work for the production of LLZO separators [34]. A typical tape casting process comprises four separate steps, namely (i) powder conditioning (pre-treatment), (ii) slurry preparation, (iii) slurry casting, and (iv) shaping, pressing, and sintering (Figure 1). Each step can be optimized to achieve the desired morphology and functionality of the resulting components. The slurry for casting composite cathodes contained LLZO as the catholyte (similar to the tape casting procedure for LLZO separators) but also two additional components, namely NMC as CAM and Li_3BO_3 (LBO) as sintering aid [35] (Figure S1). While the overall workflow was retained, significant changes were required during the preparation of the slurry to account for the differences in the chemical composition and reactivity of the additional components NMC and LBO. For example, the binder polyvinyl butyral (PVB) had to be changed due to its incompatibility with LBO. Li_3BO_3 can undergo partial dissociation in aqueous and polar solutions, leading to the formation of borate species such as $B(OH)_4^-$ and $B_2O_4^{2-}$ through reactions similar to the hydrolysis of B_2O_3 [36]. These borate species readily coordinate with hydroxyl-rich polymers such as PVB, promoting uncontrolled cross-linking and gelation that make the slurry formulation uncastable, as we show in the supporting information (Figure S2). The PVB was then replaced with carboxymethyl cellulose (CMC), a polysaccharide-based binder with a more chemically tolerant structure. Although CMC also contains hydroxyl groups, it exhibited significantly lower reactivity with borate species under the same solvent conditions, likely due to its linear, anionic backbone and weaker coordination affinity. At the same time, the concentration of the ammonium-based dispersant (BYK-180) in the slurry was reduced to avoid excessive basicity, which could otherwise promote further borate dissociation and destabilization of the slurry rheology Table 1.

Prior to slurry preparation and tape casting, the LLZO and NMC powders were ball milled to reduce particle size and achieve a more uniform distribution suitable for tape casting. Particle size distribution (PSD) analysis confirms that milling significantly shifted the PSD of both LLZO and NMC powders toward the submicron and low-micron range (Figure S3), improving the homogeneity and dispersion of the slurry. The LLZO powder was annealed in air at 750°C after ball milling to remove Li_2CO_3 formed on the particle surface due to protonation, as confirmed previously [34]. The LBO powder was only dry-ground by hand to avoid any structural or compositional changes that could result from high-energy, solvent-based ball milling. Following this optimized protocol, two different composite cathode variants were prepared, namely NMC-LLZO-LBO (46:46:8 wt%) and NMC-LBO (92:8 wt%). The LBO content was set at 8 wt.% in both configurations to minimize the effect of LBO on electrochemical performance, as LBO possesses a significantly lower lithium-ion conductivity (~2×10^{-6} S cm^{-1}) [24] than LLZO (1×10^{-3} S cm^{-1})

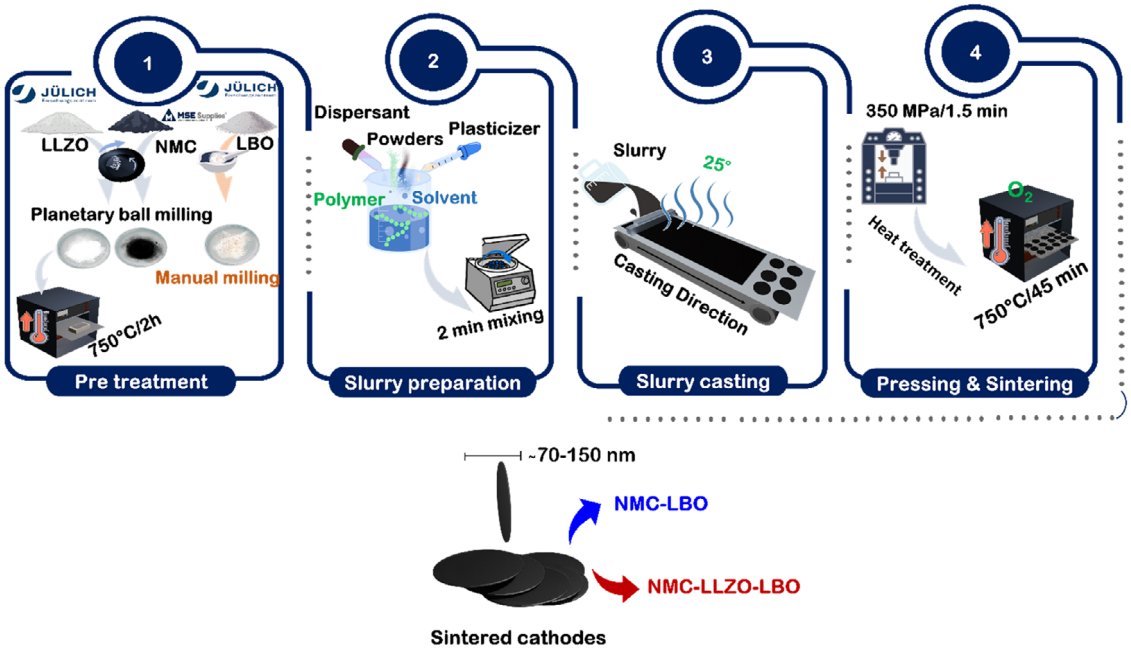

FIGURE 1 | Schematic of the composite cathode fabrication process, including powder pre-treatment, slurry preparation, tape casting, and pressing/sintering.

TABLE 1 | Slurry compositions of composite cathodes compared with the reported LLZO tape-casting formulation [34]. PVB: poly (vinyl butyral), CMC: carboxymethyl cellulose, EtOH: ethanol, MEK: methyl ethyl ketone, PEG-400: polyethylene glycol (Mn ≈ 400 g mol^{-1}), TEG-EH: Tri(ethylenglycol)bis-2-ethylhexanoate, BYK-180: polymeric dispersant.

Slurry system	Powder, wt%			Binder solution, wt%						Ref
	LLZO, wt%	NMC, wt%	LBO, wt%	Binder (type, wt%)	Solvent mixture (type, wt%)	Plasticizers, wt% (type, wt%)		Dispersant (type, wt%)	Powder: binder solution, wt%	
LLZO slurry	100	—	—	PVB (5.23)	EtOH:MEK (86.44)	PEG-400 (2.59)	TEG-EH (2.59)	BYK-180 (3.15)	1 : 0.65	[34]
NMC–LLZO–LBO slurry	46	46	8	CMC (7.07)	EtOH:MEK (84.74)	PEG-400 (3.76)	TEG-EH (3.76)	BYK-180 (0.7)	1.8 : 1	This work
NMC–LBO slurry	—	92	8	CMC (7.07)	EtOH:MEK (84.74)	PEG-400 (3.76)	TEG-EH (3.76)	BYK-180 (0.7)	1.8 : 1	

[37] and fluctuations in its concentration could otherwise lead to uncontrolled differences in ionic transport within the composite cathode. The composite cathode tapes were sintered at 750°C for 45 min in a pure oxygen atmosphere to preserve Ni in the oxidation state Ni^{3+} and suppress the formation of oxygen-deficient reduced phases that could impair the electrochemical performance [22, 32]. To ensure controlled removal of organic components and prevent tape deformation, the heating profile was optimized based on thermogravimetric analysis. The temperature was slowly increased from room temperature to 600°C at a rate of 2°C min^{-1}, with intermediate dwell steps of 15 min at 200°C and 600°C. These steps allow for gradual evaporation and decomposition of residual solvents and polymeric binders before the onset of ceramic densification and promote homogeneous mass loss across the entire tape thickness. This controlled burnout minimizes gas pressure build-up, reduces internal stress gradients, and thus suppresses warping or deformation of the tapes during subsequent high-temperature sintering.

After tape casting and drying, uniform green tapes were obtained for both composite cathode compositions (NMC-LBO and NMC-LLZO-LBO). The green tapes exhibited excellent flexibility and mechanical integrity. The dried green tapes could be handled and punched into discs of 10 mm without cracking and showed uniform thickness across the entire cast area, as shown in Figure 2a,e. After sintering, free-standing, fully ceramic composite cathodes with a diameter of 9.4 mm were obtained. Both composite cathode tapes (NMC-LBO and NMC-LLZO-LBO) exhibited reasonable mechanical integrity and remained visibly flat, as can be seen in the photographs (Figure 2b,f). Chromatic white light topography further confirms a uniform surface topography at the microscale (Figure 2e,f) and shows uniform, flat surfaces without significant warping or delamination. The successful retention of tape geometry underscores the effectiveness of the optimized slurry formulation and controlled sintering conditions. Cross-sectional scanning electron microscopy (SEM) images showed comparable final thicknesses of approximately 90 µm for both tapes (Figure 2d,h). This dimensional consistency is particularly important to ensure uniform current distribution and minimize variations in cell performance during electrochemical testing.

SEM analysis of the fracture surfaces shows a densely packed granular microstructure for both NMC-LBO and NMC-LLZO-LBO composite cathodes (Figure 3a,b). The backscattered electron SEM images visualize the different phases within the composite cathodes based on their material (Z) contrast. LLZO appears as very bright particles, while the NMC particles are light gray. Due to its low average atomic number, the LBO phase appears as dark gray regions surrounding the LLZO and NMC particles, which is confirmed by energy-dispersive X-ray spectroscopy (EDX) (Figure S4). The spatial distribution and morphology of these LBO-rich regions suggest liquid phase-assisted densification during sintering. Moreover, they appear similar in both composites, confirming that LBO does not undergo any detectable reactions with the other components under the processing conditions applied. SEM/EDX does not detect any additional secondary phases with distinct morphology or material contrast at the investigated magnifications. This suggests that all secondary phases identified by XRD are either present in low volume fractions or below the spatial resolution of SEM/EDX.

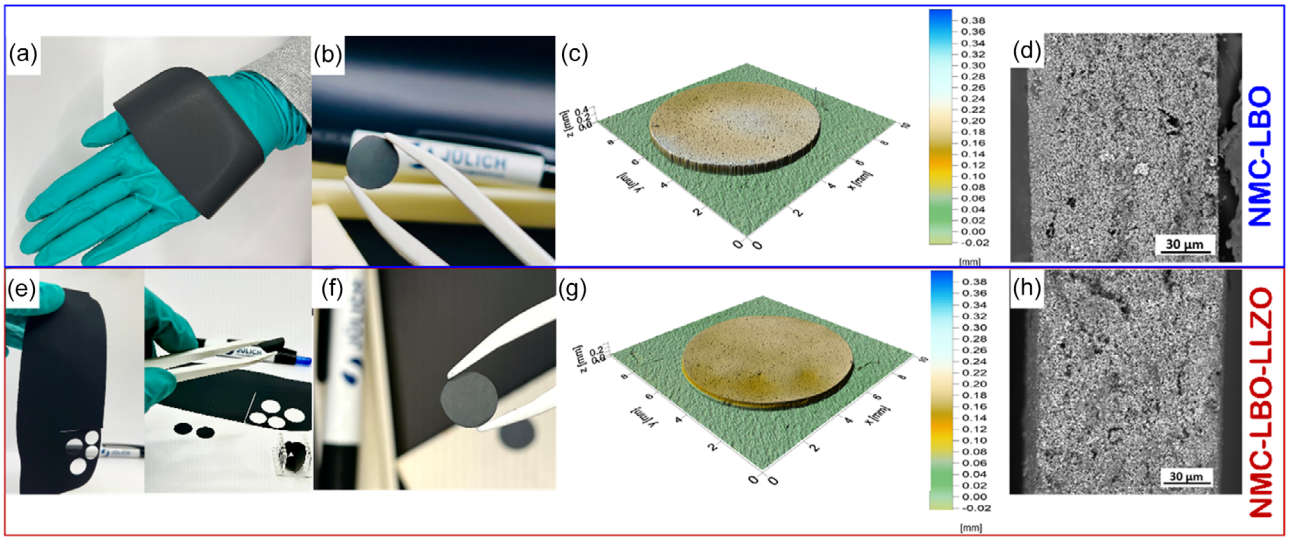

FIGURE 2 | Morphological comparison of as prepared ("green") and sintered composite cathodes. NMC-LBO (top, blue frame) and NMC-LLZO-LBO (below, red frame): (a) and (e) photographs of the green tapes; (b) and (f) photographs of the sintered tapes at 750°C in pure oxygen; (c) and (g) white light topography showing flatness and thickness uniformity of sintered tapes; (d) and (h) SEM images of cross-sections of cathode tapes after sintering.

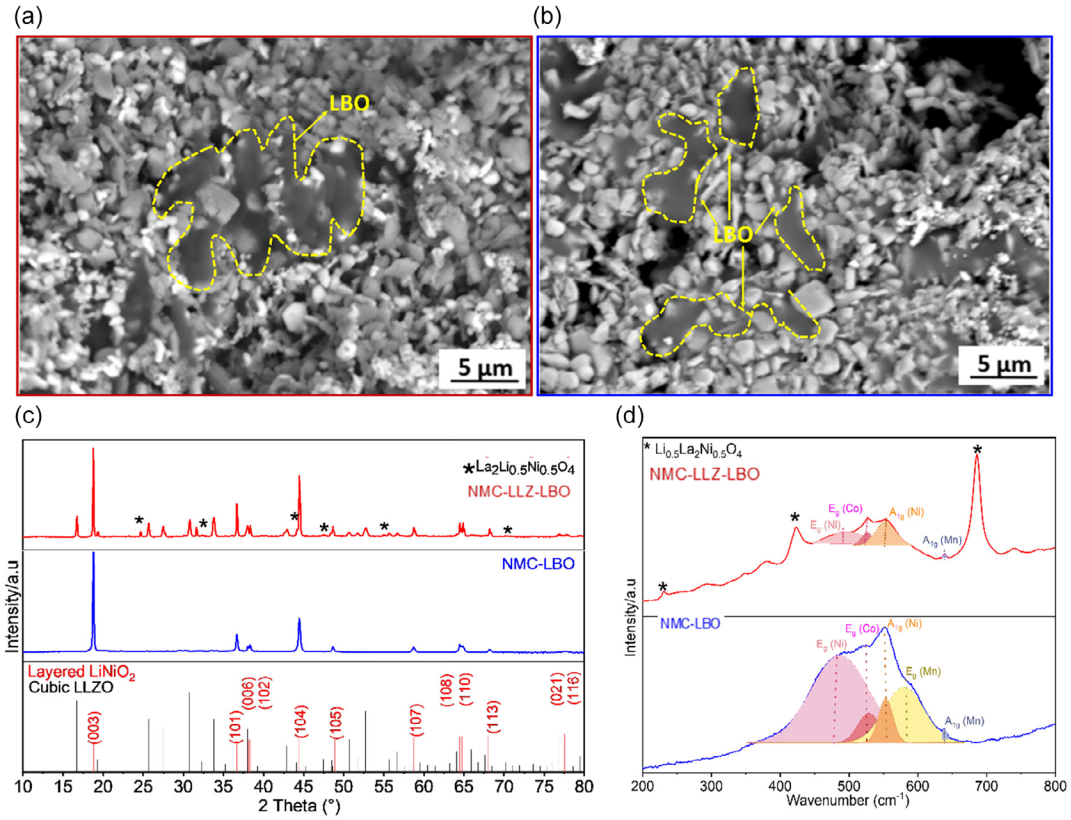

FIGURE 3 | Backscattered electron SEM images of (a) fracture surfaces of the NMC-LLZO-LBO and (b) NMC-LBO composite cathodes sintered at 750°C in a pure oxygen atmosphere; (c) XRD patterns and (d) Raman spectra of the composite cathodes shown in (a) and (b).

X-ray diffraction (XRD) and Raman spectroscopy mapping were performed on the sintered samples (Figure 3c,d). The XRD pattern of the NMC-LBO composite shows only reflections associated with the layered NMC phase. No reflections associated with crystalline LBO are detected, which is probably due to its low weight ratio and amorphous nature after sintering. In contrast, the XRD pattern of the NMC-LLZO-LBO composite shows several additional peaks in addition to cubic LLZO and layered NMC, which can be indexed to the $La_2Li_{0.5}Ni_{0.5}O_4$ phase, consistent with previous published work [21, 38]. However, cubic

LLZO and NMC are still the main phases after co-sintering. Importantly, in both composite cathodes, the characteristic diffraction features of the hexagonal layered NMC structure are preserved after tape casting and sintering. The layered NMC structure remains intact in both composites, as evidenced by the clear splitting of the (006)/(012) and (108)/(110) reflections, confirming a well-ordered hexagonal layered structure [39, 40]. A quantitative evaluation of the (003)/(104) intensity ratio is not reliable for the LLZO-containing composite due to the overlap of the NMC (104) reflection with a diffraction peak of LLZO. Therefore, the structural changes were instead evaluated based on the lattice parameters. Le Bail refinement of the powder XRD patterns reveals a slight decrease in the c/a lattice parameter ratio for both NMC-LBO and NMC-LLZO-LBO (4.94) compared to the ball-milled NMC (4.95) (Figure S4), indicating only a slight increase in cation disorder (antisite defects, Ni^{2+} occupying Li sites) after tape casting and sintering. The presence of LLZO in the composite cathode had no effect on the cation mixing.

To further elucidate the structural evolution during thermal treatment, XRD and Raman spectroscopy were performed on the NMC-LLZO-LBO composite cathodes sintered at different temperatures of 200°C, 400°C, and 600°C (Figure S5). The results confirm that the formation of the secondary $La_2Li_{0.5}Ni_{0.5}O_4$ phase only occurs at temperatures above 600°C. This phase evolution is accompanied by a significant suppression and eventual disappearance of the Raman bands typically observed around 250–350 cm^{-1} [41], suggesting that the formation of $La_2Li_{0.5}Ni_{0.5}O_4$ occurs at the expense of LLZO decomposition.

Raman mapping spectroscopy provides further insights into the structure evolution after cosintering. In the NMC-LBO cathode, characteristic Raman bands of the layered structure are clearly visible in the range of 400–600 cm^{-1} [42], including well-resolved peaks corresponding to E_g(Ni), E_g(Co), A_{1g}(Ni), and E_g(Mn) [42, 43]. The presence of a relatively strong A_{1g}(Ni) mode could indicate a minor degree of cation mixing, which is consistent with Le Bail refinement. On the other hand, the Raman spectrum of the NMC-LLZO-LBO composite shows broad and significantly attenuated NMC signals. It is noteworthy that the A_{1g}(Ni) mode shows a significant reduction in intensity, and the A_{1g}(Ni)/E_g(Co) intensity ratio is relatively reduced. This is indicative of increased cation disorder within the NMC structure, likely caused by the abovementioned antisite defects or Ni leaching from the layered structure, which disrupts the layered symmetry and attenuates the vibrational modes. The NMC spectral distortions are also accompanied by the formation of a secondary phase, as evidenced by the appearance of sharp peaks around 220, 410, and 689 cm^{-1}, which correspond to the vibrational modes reported for $La_2Li_{0.5}Ni_{0.5}O_4$ [21, 28] and are consistent with the XRD results. We can therefore confirm that a La-Ni-O secondary phase is formed at the expense of Ni leaching from the NMC structure, which probably reacts with LLZO during cosintering at 750°C.

To evaluate the electrochemical performance of the NMC-LBO and NMC-LLZO-LBO cathodes, they were incorporated into hybrid polymer-ceramic SSBs with lithium-metal anodes. A solution of poly(ε-caprolactone) grafted cyclodextrin (GCD-PCL) polymer and lithium bis(trifluoromethanesulfonyl)imide (LiTFSI) salt in THF was infiltrated into the composite cathode tapes and used as a connection layer between the composite cathode tape and the dense, pre-sintered LLZO:Ta separator. GCD-PCL was selected due to its low interfacial charge transfer resistance and stability at high voltages up to 4.3 V, ensuring compatibility with Ni-rich NMC during electrochemical cycling [44]. To obtain a full cell, a Li metal anode was attached to the other side of the dense LLZO:Ta separator.

Various composite cathode configurations were tested to systematically evaluate the interaction between ion and electron transport in the composite cathodes. The NMC-LBO cathode, which has low total ionic conductivity but high phase purity, is compared with the NMC-LLZO-LBO variant, which should have significantly higher ionic conductivity due to the presence of LLZO, but also contains a secondary phase whose effects on electrochemical performance have not yet been explored. In addition, given the inherently low electronic conductivity of the NMC811 (10^{-8} S cm^{-2}) [33], 5 wt% carbon black was added to the GCD-PCL electrolyte to improve the electron conduction pathways within the composite cathode. This resulted in four cathode configurations: NMC-LBO, NMC-LBO + C, NMC-LLZO-LBO, and NMC-LLZO-LBO + C. A schematic representation of the four full-cell configurations is provided in (Figure 4).

The designed cell configurations enable the evaluation of different transport contributions: (I) The comparison of NMC-LBO with NMC-LLZO-LBO shows the influence of the ionic conductivity introduced by the Li-ion conductor LLZO. (II) Comparing NMC-LBO with and without carbon deconvolutes the effect of improved electronic conductivity. (III) Comparing the two carbon-containing composites helps to assess whether the addition of carbon can compensate for the performance limitations caused by the secondary phase in the LLZO-containing cathode.

The backscattered electron SEM images of the fractured half-cell (Figure 5) show a continuous polymer interlayer that conformally bridges the composite cathode and the LLZO separator. The polymer infiltrates the porous cathode and fills the residual porosity, indicating good adhesion and intimate interfacial contact. Similar infiltration behavior is observed in both cathode configurations, which is consistent with their comparable

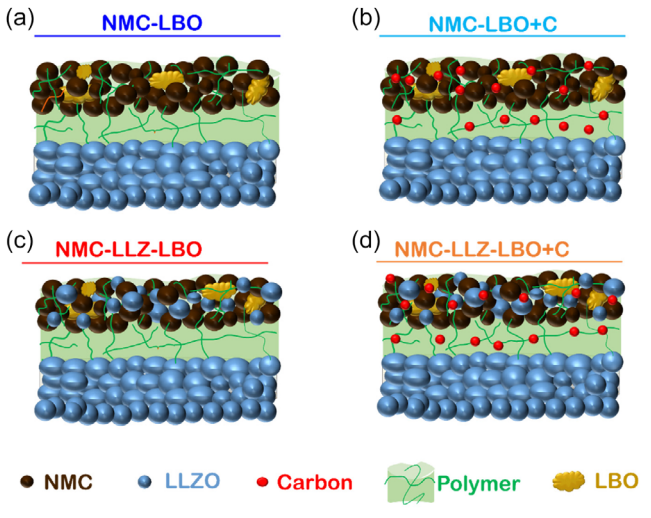

FIGURE 4 | Schematic illustration of the four cell configurations investigated in this work: (a) NMC-LBO based cell; (b) NMC-LLZO-LBO based cell; (c) NMC-LBO + C based cell; and (d) NMC-LLZO-LBO + C based cell.

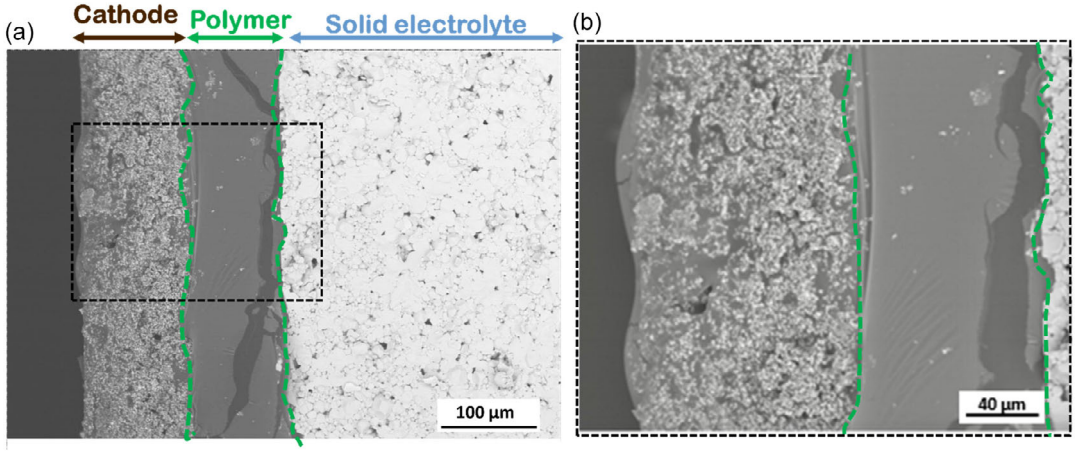

FIGURE 5 | (a) Backscattered electron SEM images of fractured half cell (NMC-LLZO-LBO), showing the polymer interlayer between the composite cathode and the solid LLZO separator. (b) Magnified image of the boxed region, highlighting the polymer infiltrated composite cathode.

relative densities of 79% for NMC-LBO and 81% for NMC-LLZO-LBO, suggesting a similar degree of infiltration.

The hybrid polymer-ceramic SSBs were characterized by galvanostatic charge–discharge experiments at a constant current density of 40 µA/cm^2 at 60°C. When comparing the first charge–discharge profiles, all cells exhibit defined plateaus within the expected voltage range of Ni-rich NMC, indicating that the optimized slurry preparation and cosintering do not impair the electrochemical activity of the CAM (Figure 6). This is further supported by the differential capacity analysis (Figure S8), which shows distinct redox peaks at potentials typically associated with Ni-rich NMC, confirming reversible lithium extraction and insertion. The NMC-LLZO-LBO cell delivered a higher initial discharge capacity of 134 mAhg^{-1} (~63% utilization) and lower polarization compared to NMC-LBO (Figure 6a,b), which delivered only 46 mAhg^{-1} (~21% utilization), accompanied by higher polarization and significant voltage hysteresis, indicating higher total resistance of the electrode layer. With carbon addition, the NMC-LBO + C configuration showed the best performance (Figure 6c), achieving an initial areal discharge capacity of 6.1 mAh cm^{-2} and a gravimetric discharge capacity of 205 mAh g^{-1} corresponding to ~97% capacity utilization relative to the expected practical capacity of Ni-rich NMC811 (~210 mAh g^{-1}) [45]. This is accompanied by reduced polarization and improved electrochemical reversibility, mainly due to the improved electronic conductivity provided by the carbon network. We assume that the carbon network improves total electronic conductivity of the composite cathodes so that previously isolated regions in the NMC-LBO cathode with an extremely high NMC loading of around 26 mg/cm^2 become accessible. The NMC-LLZO-LBO + C (Figure 6d) cell also showed improved performance compared to its carbon-free counterpart, achieving 169 mAh g^{-1} (80% utilization) at slightly lower polarization. However, despite this improvement, its overall performance remained lower compared to the NMC-LBO + C composite cathode. It is noteworthy that the electrochemical performance and both the areal and gravimetric discharge capacities of the NMC-LBO + C cell exceed the values typically reported for NMC-based composite cathodes produced by cosintering at elevated temperatures [14, 26, 29, 46], where capacity utilization is often limited to comparable or lower loadings due to interfacial degradation and transport limitations. This performance advantage becomes even more apparent when compared to pure polymer-based cell configurations. In a recent study [47] on conventional NMC622 electrodes, which were infiltrated with the same GCD-PCL polymer electrolyte using a more elaborate technique and also cycled at 60°C, a gravimetric discharge capacity of only 94 mAh g^{-1} at 0.05 C was reported for an electrode loading of 6 mg cm^{-2}, while the cathodes with the highest loading (12 mg cm^{-2}, approximately half the areal loading of our NMC-LBO + C cathode) achieved only ~80% of the theoretical discharge capacity at the same rate. These results confirm that the operating temperature of 60°C is not the decisive performance factor in our system, as it is equally required by the polymer electrolyte in both architectures, and demonstrate that the hybrid, ceramic-supported design enables significantly higher utilization of the active material at high surface loading than a purely polymer-based approach. The markedly different effect of carbon in the two systems suggests that electron transport is the main limiting factor in the NMC-LBO cathode, while in LLZO-containing cathodes, the electrochemical performance is likely determined by more complex interfacial and chemical constraints. In the latter case, multiple ceramic–ceramic interfaces and secondary phases formed during cosintering as confirmed by XRD and Raman spectroscopy, likely limit the effective interaction between carbon and the NMC particles, reducing the benefit of enhanced electronic conductivity. These results suggest that while LLZO may facilitate the initial electrochemical activation of NMC in the thick composite cathode by providing ion-conducting pathways, its presence does not necessarily lead to higher capacity utilization when interfacial resistances dominate. Instead, improved electronic percolation alone can effectively improve the capacity utilization of NMC, even when LLZO is not present in the composite cathode.

Electrochemical impedance spectroscopy (EIS) (Figure 7) corroborates the trends observed during galvanostatic cycling (Figure 6). The impedance spectra were fitted using equivalent circuits, as shown in Figure 7a,b. The NMC-LLZO-LBO cathodes, both with and without carbon, exhibit three overlapping semicircles distributed across the high, mid, and low-frequency ranges (Figure 7a). The high-frequency feature ($C_1 \approx 10^{-10}$ F) is consistent with contributions from the bulk and grain boundaries impedance of LLZO [13, 48], while the mid-frequency and low-frequency semicircles

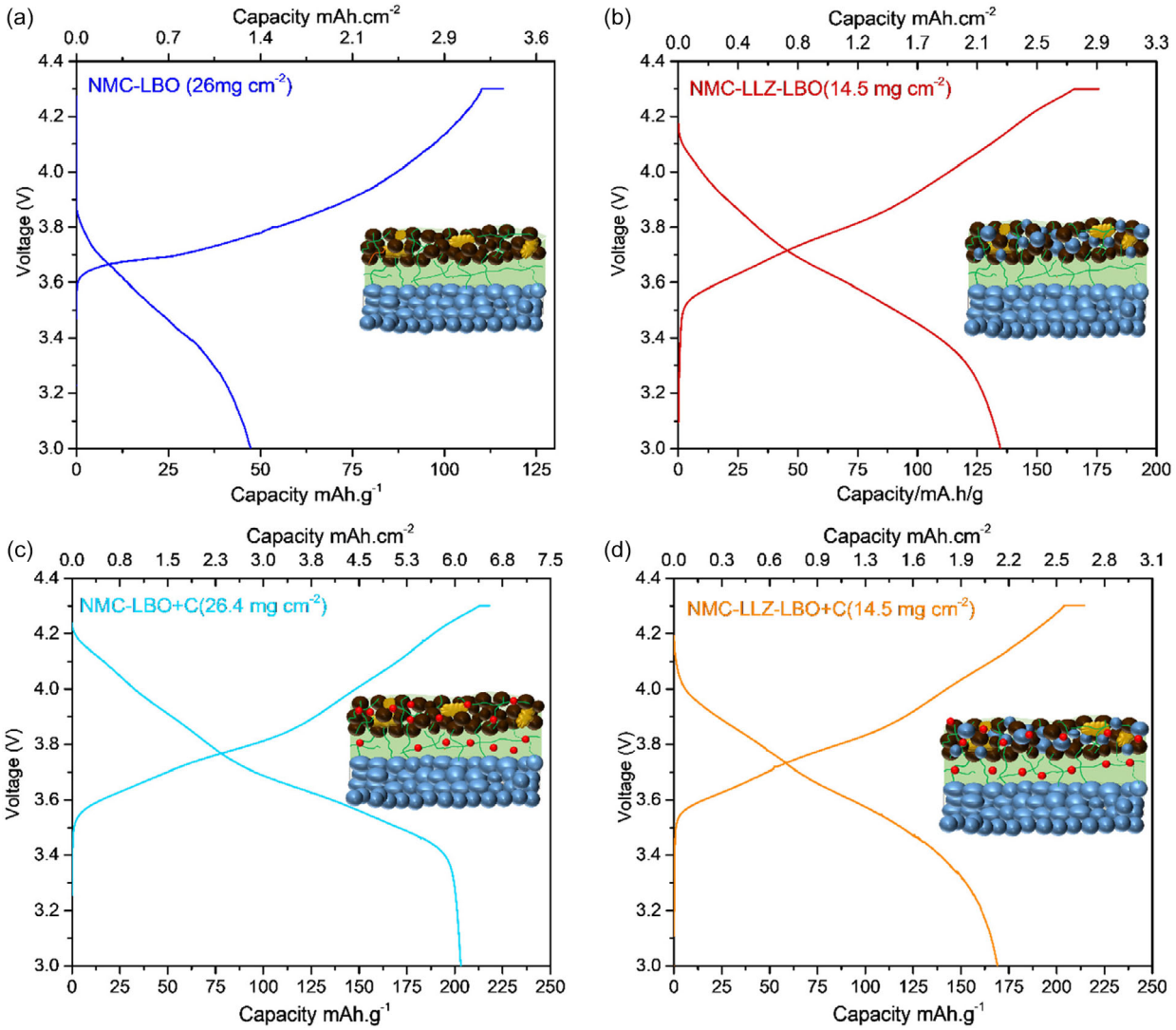

FIGURE 6 | Charge–discharge voltage profiles (first cycle) of the hybrid, polymer-ceramic SSBs with the four different composite cathode configurations at 60°C and 0.01C: (a) NMC-LBO based cell (dark blue); (b) NMC-LLZO-LBO based cell (red); (c) NMC-LBO + C based cell (light blue); and (d) NMC-LLZO-LBO + C based cell (orange).

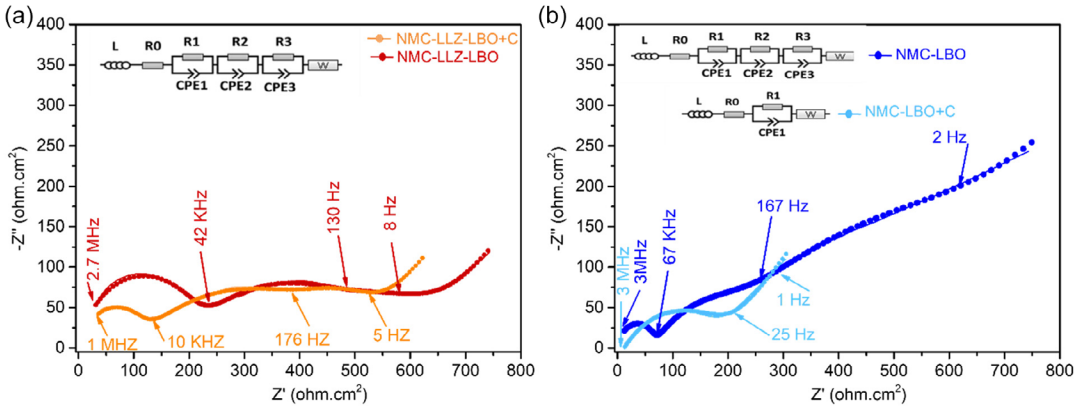

FIGURE 7 | Nyquist plots of the EIS spectra of the of the hybrid polymer-ceramic SSBs before cycling measured at 60°C and the equivalent circuits used for fitting: (a) NMC-LLZO-LBO and NMC-LLZO-LBO + C based cells and (b) NMC-LBO and NMC-LBO + C based cells.

($C_2 \approx 10^{-4}$–10^{-5} F) most likely reflect interfacial processes involving the interfaces between the polymer and the NMC, the LLZO, and possible secondary phases [13]. The NMC-LBO cell without carbon also shows three strongly overlapping semicircles, but with markedly different effective capacitances. The high and mid-frequency semicircles have larger capacitances

(C_1 and $C_2 \approx 10^{-7}$ F), suggesting contributions from the CAM [31], while the low-frequency semicircle ($C_3 \approx 10^{-5}$ F) is related to slow Li^+ transport across the polymer interface [13]. The different capacitance ranges indicate that the NMC-LLZO-LBO and NMC-LBO cathodes are likely controlled by different rate-determining mechanisms. Due to the inherent complexity of hybrid polymer-ceramic composite cathodes with multiple interfaces, a detailed deconvolution of individual impedance contributions is not readily possible. Therefore, the comparison here is based on the total cell resistance extracted from the fitting of the equivalent circuit model (Table S2). The total cell resistance of the NMC-LLZO-LBO cell is 654 Ω cm^2, which is significantly lower than that of the NMC-LBO cell (2182 Ω cm^2), consistent with a reduced overall ionic transport limitation when LLZO is present as a catholyte. This also confirms that the NMC-LLZO-LBO cathode remains more conductive overall than the NMC-LBO cathode when assembled in an identical cell configuration, despite the secondary phases observed previously. The poor capacity utilization of the NMC-LBO cathode is likely related to impeded electrochemical exchange caused by the low ionic and electronic conductivity in the cathode. The addition of carbon reduces the total resistance of the NMC-LLZO-LBO + C composite to 541 Ω cm^2, while NMC-LBO + C exhibits the lowest total resistance of all cathode configurations investigated within this work (308 Ω cm^2). The total cell resistance is one order of magnitude lower than that of the NMC-LBO cathode without carbon. The reduced resistance in the NMC-LBO + C configuration is accompanied by a single depressed semicircle indicating a more homogeneous impedance response, possibly dominated by improved electronic percolation. The greatly reduced resistance is consistent with the high initial capacities and low polarization observed during the first cycle. The EIS results confirm that improved electronic conductivity can compensate for the limited ionic conductivity in the absence of LLZO. In contrast, the addition of carbon to LLZO-containing cathodes affected by secondary phase formation has a more limited effect on reducing interfacial resistance and improving overall electrochemical performance.

All composite cathode configurations examined show a significant loss of capacity during prolonged cycling (Figure 8a). Among all systems, the NMC-LBO + C cathode exhibits the most stable early cycling behavior, retaining 95% of its initial capacity with a Coulombic efficiency of over 90% in the first five cycles. This performance exceeds the capacity retention reported for comparable NMC-based composite cathodes in similar hybrid solid-state configurations and is even better than the cycling stability of thinner cathode layers [14, 26]. Nevertheless, further cycling leads to a continuous capacity decline, and all systems suffer from severe capacity degradation to only 20 $mAhg^{-1}$ within less than ten cycles, which is comparable to the degradation rate typically reported for oxide-based composite cathodes [13, 31]. To gain further insights into the degradation process, EIS was performed again after the third cycle (Figure 8c,d). All cells show a significant increase in total resistance after three cycles. In particular, the carbon-free NMC-LBO cell exhibits a sharp increase in the low-frequency impedance contribution,

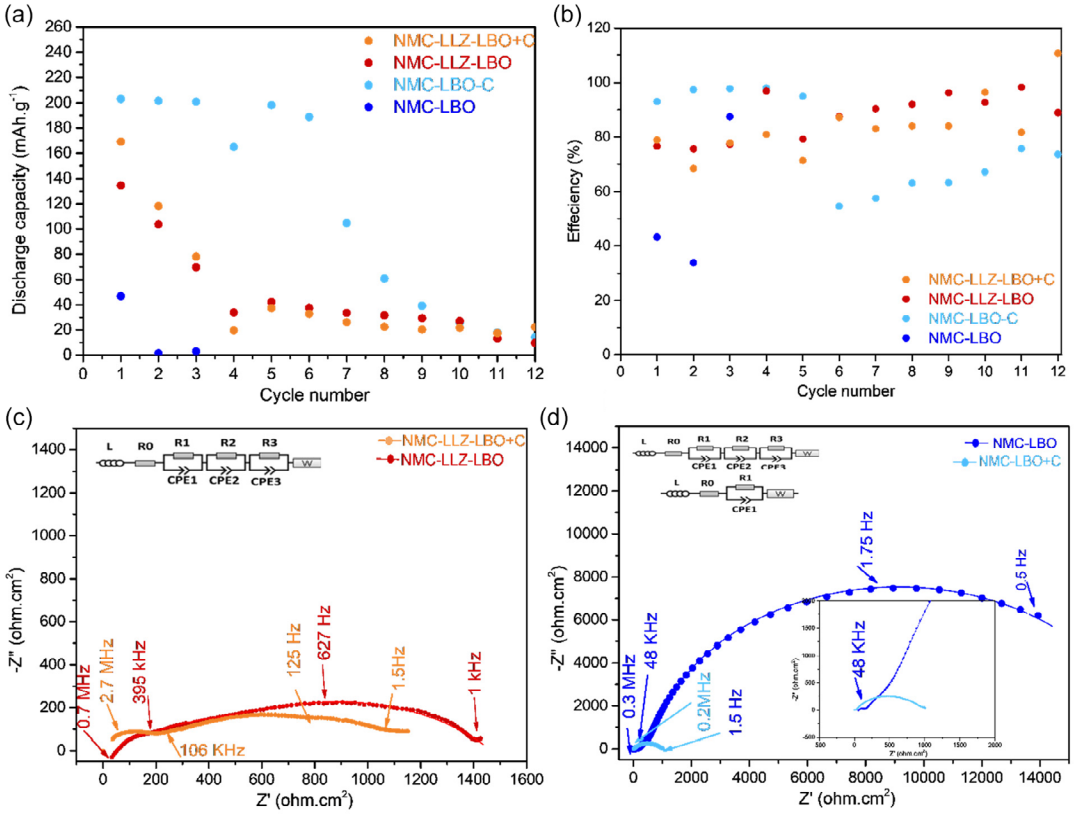

FIGURE 8 | (a) Discharge capacity of the hybrid, polymer-ceramic SSBs with the four different composite cathode configurations for the first 12 cycles at 60°C and 0.01C; (b) Coulombic efficiency for the cycles shown in (a); (c) EIS spectra of the NMC-LLZ-LBO and NMC-LLZ-LBO + C configurations after the third cycle, and (d) EIS spectra of the NMC-LBO and NMC-LBO + C configuration after the third cycle.

indicating an increase in the effective charge transfer resistance at the interfaces already in the first cycles. This behavior is consistent with the intrinsically limited ion and electron transport in this cathode configuration, leading to a rapid decay in electrochemical activity. It is evident that the presence of LLZO in the NMC-LLZO-LBO cathodes mitigates such early failure. LLZO-containing cells exhibit a monotonic capacity decay accompanied by a comparable increase in impedance, dominated by contributions in the mid-to-low frequency range, suggesting that their electrochemical performance is determined by the progressive build-up of interfacial resistances that cannot be significantly mitigated by improved electronic percolation alone. Similar correlations between monotonic capacity fading and the build-up of interfacial impedance during cycling have been reported for LLZO-based composite cathodes with comparable composition, suggesting an interface-dominated degradation process [14, 26]. The addition of carbon has only a limited influence on the short-term cycling stability of the NMC-LBO + C cathode. It is noteworthy that this cell exhibits a nonmonotonic capacity evolution during the initial cycles (Figure 8a), suggesting that the observed capacity fluctuations are not due to purely progressive build-up of interfacial resistances or a continuous loss of electrochemical activity. Rather, the increase in cell resistance after the third cycle indicates changes in the electrochemically accessible fraction of the CAM. A plausible mechanism is a mechanically induced loss of contact within the composite cathode, in which chemo-mechanical volume changes during cycling locally damage interfaces or isolate parts of the NMC from the percolating transport network. Similar capacity decay trends have been observed in LCO-LLZO composite cathodes fabricated by tape casting, where the loss of capacity during cycling was mainly attributed to electro-chemo-mechanical degradation caused by volume changes in LCO particles during lithiation and delithiation [13, 31]. A comparable mechanism could also contribute to the performance degradation observed here, which can be exacerbated by additional degradation processes of Ni-rich NMC [49–51], including greater lattice strain, volume change, and potential interfacial reactivity.

The Raman spectra of the carbon-free NMC-LBO cathodes after cycling (Figure S10) show that the NMC and LBO phases remain largely preserved. The characteristic modes of the layered NMC structure are still clearly distinguishable. The Ni-O vibrational modes E_g(Ni) and A_{1g}(Ni) are still present and show only a slight peak broadening. Importantly, the A_{1g}(Ni)/E_g intensity ratio does not show any significant additional decrease compared to the as-prepared cathodes. This suggests that, in the absence of LLZO, the layered NMC framework remains structurally stable during cycling. The observed capacity fading is therefore more likely associated with mechanical degradation rather than chemically driven interfacial reactions.

In contrast, the cycled NMC-LLZO-LBO composite shows further attenuation and broadening of the NMC-related Raman peaks, with the intensity of the E_g(Ni) mode decreasing during cycling. The characteristic secondary-phase peaks assigned to $La_2Li_{0.5}Ni_{0.5}O_4$ remain clearly visible, their intensity and position do not change, indicating the La-Li-Ni-O phase formed during sintering does not evolve further during cycling. The progressive suppression of the vibrational modes of the layered NMC structure indicates ongoing structural degradation, likely associated with the local symmetry distortion at the NMC-LLZO interface. The stability of the $La_2Li_{0.5}Ni_{0.5}O_4$ phase further supports that this interfacial reaction product remains electrochemically inactive and not contributes to impedance growth during cycling. However, it should be noted that the electrochemical and mechanical instability of the polymer interlayer upon repeated cycling can contribute to the capacity decay. This has also been observed in pure-polymer-based cells. Conventional cathodes with a high loading of 12 mg cm^{-2} (roughly half the areal loading of our highest-performing cathode), which were infiltrated with the same GCD-PCL polymer, also exhibit a significant capacity decay within the first 10 cycles [47], suggesting that rapid capacity fading at high areal loading is not specific to the hybrid ceramic architecture but reflects a more general challenge common to both approaches. Therefore, further targeted studies are needed in the future to examine the cycling stability of thick NMC composite cathode in such hybrid-ceramic cells.

The EIS characterization was also supported by galvanostatic intermittent titration technique (GITT) measurements. GITT measurements were conducted at 60°C with a current density of 40 μA·cm^{-2}, consisting of 3 hr current steps followed by 1 hr relaxation intervals. EIS was performed after each titration step. The apparent diffusion coefficient D was calculated using Equation (1) [52] where t (s) is the dwell time, mb (g) is the total mass loading, S (cm^2) is the cathode surface, M_B (g mol^{-1}) is the molecular weight, ΔE_s the steady-state voltage change during the current step, and ΔE_t is the total voltage change during the current pulse.

$$D = 4/t\,\pi(mb\,V_M/M_B\,S)^2(\Delta E_s/\Delta E_t)^2 \quad (1)$$

Despite the relatively long relaxation times applied during the GITT measurements, the voltage response in the GITT profiles is dominated by abrupt IR drops and only limited diffusion-controlled relaxation (Figure 9a). This behavior indicates that the GITT profiles primarily reflect instantaneous polarization and transport effects at the electrode level rather than diffusion-controlled processes. Accordingly, the diffusion coefficients derived from these measurements are treated as apparent parameters that describe effective transport kinetics in the entire cathode and not the intrinsic solid-state lithium diffusion in the active materials.

The amplitude of the instantaneous IR drop after current shutdown is largest for the NMC-LBO electrode, indicating significant electrode resistance due to the low ionic conductivity of LBO and the low electronic conductivity of the composite electrode morphology. The incorporation of LLZO into the composite cathode (NMC-LLZO-LBO) moderately reduces the IR drop amplitudes compared to NMC-LBO, suggesting that LLZO provides higher ionic conductivity and thus lower overall resistance of the electrode. In LLZO-containing cathodes, the addition of carbon leads to a further (albeit slight) reduction in the IR-drop amplitude and marginally higher apparent diffusion coefficients. This observation is consistent with the EIS results and suggests that electrode kinetics are primarily determined by high interfacial resistances that cannot be significantly reduced by improved electronic percolation alone. In contrast, the addition of carbon to the LLZO-free NMC-LBO + C cathode results in a significant reduction in the IR-drop amplitude and yields the highest apparent lithium diffusion coefficients over the

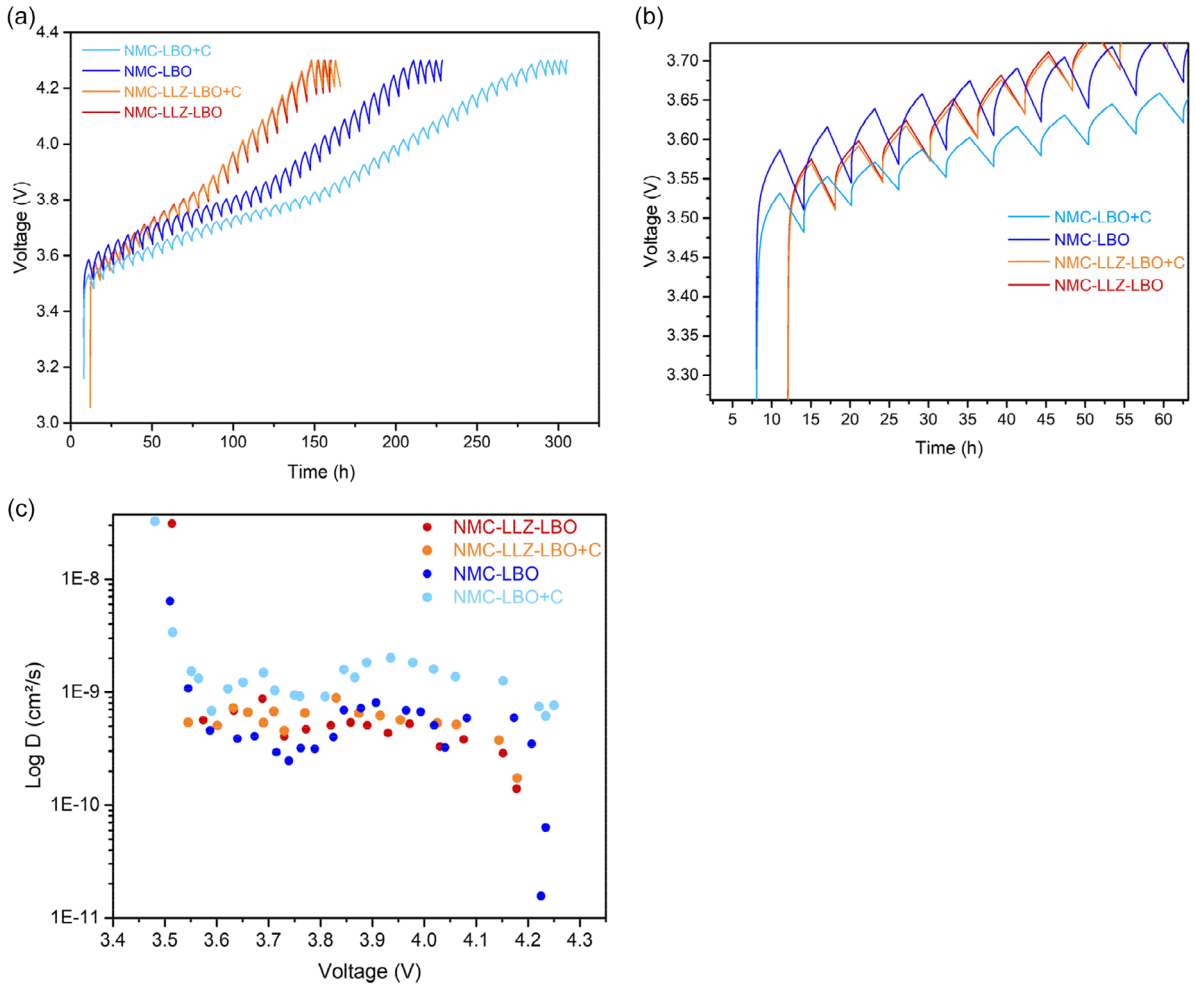

FIGURE 9 | (a) GITT voltage profiles for NMC-LBO, NMC-LBO + C, NMC-LLZO-LBO, and NMC-LLZOLBO + C at 60°C; (b) magnified GITT voltage profiles between 3.3 and 3.7 V for the composite cathode configurations shown in (a); (c) apparent Li^+ diffusion coefficients for the four composite cathode configurations calculated from the GITT profiles.

entire SOC range (Figure 9b). This strong correlation suggests that, in the absence of LLZO, electrode resistance is dominated by electronic contribution, which can be effectively improved by adding carbon. We therefore conclude that the incorporation of LLZO primarily improves ion transport, but at the same time introduces interfacial limitations that restrict further kinetic gains. In contrast, the addition of carbon reduces electronic resistance and improves exchange kinetics in NMC–LBO + C cathodes, making it the most effective strategy for improving NMC capacity utilization in thick composite cathodes without LLZO incorporation.

Analysis of distribution of relaxation times (DRT) (Figure S9) confirms the trends observed in the GITT measurements. The main difference between the cathode systems studied is reflected in the evolution of the mid-frequency relaxation process P3 (10^4–10^2 Hz), which is sensitive to cathode chemistry and interfacial transport within the cathode [53]. In LLZO-containing cathodes (NMC-LLZO-LBO), the P3 process broadens with increasing state of charge, probably due to the continuously increasing interfacial resistance. Although the addition of carbon partially suppresses this contribution, it still remains, suggesting that transport in LLZO-containing cathodes is predominantly limited by chemically and structurally induced interfacial effects.

3 | Conclusion

This work demonstrates for the first time a process for manufacturing electrochemically active, free-standing NMC-based composite cathodes using a scalable, industrially relevant tape casting process. We have succeeded in optimizing slurry composition to enable reproducible casting of 90 µm thick composite cathodes containing NMC, LLZO and LBO without significant material degradation. Structural and spectroscopic analyses confirm that the hexagonal layer structure of NMC and the cubic LLZO phase are largely retained after processing, however, cosintering of LLZO, NMC, and LBO as a sintering aid leads to the formation of $La_2Li_{0.5}Ni_{0.5}O_4$ as secondary phase even at a reduced temperature of only 750°C.

The composite cathodes were electrochemically active when tested in hybrid, polymer-ceramic SSBs with a Li metal anode and a dense LLZO separator. A systematic comparison between LLZO-containing and LLZO-free composite cathode architectures shows that the incorporation of LLZO enables improved electrochemical performance by providing ionic transport pathways in the thick composite cathodes but at the same time introduces interfacial constraints due to the secondary phases formed during cosintering, which limit effective capacity utilization. As a result, both NMC-LLZO-LBO and NMC-LLZO-LBO + C

cathodes exhibit only moderate active material utilization. In contrast, the LLZO-free NMC-LBO cathodes remain largely inactive and exhibited the lowest CAM utilization due to the absence of both ionically and electronically conductive pathways. However, by adding carbon, the NMC-LBO + C system even outperformed the NMC-LLZO-LBO + C system, delivering the highest capacity of all composite cathode compositions investigated in this study. An initial discharge capacity of more than 200 mAh g^{-1} and 6 mAh cm^{-2} was achieved, corresponding to a capacity utilization of almost 100%. In addition, this cell showed the highest capacity retention after 6 cycles. The combination of galvanostatic cycling, GITT, and DRT analyses shows that the performance of these thick composite cathodes is determined by the balance between ionic and electronic conductivity. While LLZO addition improves ionic transport, the low electronic conductivity and the interface limitations constrain electrode performance, while improved electronic percolation effectively enhances NMC utilization in LLZO-free architectures. These results underscore that the incorporation of LLZO alone is not sufficient to ensure high capacity utilization in thick NMC composite cathodes and highlight the importance of interface-aware cathode design for oxide-ceramic SSBs.

Based on the results of postmortem Raman spectroscopy and electrochemical analysis, we suggest that electro-chemo-mechanical degradation is the primary cause of capacity fading in composite cathodes, both with and without LLZO; therefore, improving the mechanical cohesion of the electrodes under cycling-induced strain should be the main objective. This can be achieved, for example, by reducing the CAM particle size or by using NMC particles with concentration gradients to reduce intergranular cracking and minimize the cumulative stress caused by the CAM volume change. Another possibility is also to optimize the protocol for polymer infiltration, for example, using heating or curing techniques that ensure a conformal CAM/catholyte interface and better compensate for cycling-induced volumetric stresses.

In addition to chemo-mechanical degradation, LLZO-containing cathodes exhibit another degradation pathway related to reactions at the CAM/LLZO interface. For these systems, it is therefore expected that suppressing the formation of $La_2Li_{0.5}Ni_{0.5}O_4$ during sintering would improve electrode performance. To prevent the formation of secondary phases, the use of protective surface coatings on LLZO and NMC particles (e.g., $LiNbO_3$ or Li_3PO_4), as well as fast and low-temperature sintering methods such as field-assisted sintering (FAST/SPS) should be investigated.

Our study demonstrates the possibility of scalable fabrication of freestanding LLZO- NMC cathode layers, which show high areal initial specific capacities. However, the cycling stability of the cathode layers obtained is still insufficient and should be the next frontier. Previously published studies show that the performance of NMC-LLZO composite cathodes strongly depends on several factors, including the NMC composition, the type and concentration of dopants in the LLZO structure, the coating of the NMC powder, the microstructure of the cathodes, the ionic and electronic conductivity of the cathode layer, and the type of processing, including the sintering technique, which should be investigated to increase the cycling stability of ceramic cathodes.

4 | Experimental Section

4.1 | Synthesis and Powder Conditioning

The SSE powder $Li_{6.45}Al_{0.05}La_3Zr_{1.6}Ta_{0.4}O_{12}$ (LLZO:Ta), which was used for the fabrication of tape cast cathodes and dense separators described in this work, was prepared via solid-state synthesis as described elsewhere. Stoichiometric amounts of $LiOH{\cdot}H_2O$ (Applichem, 99%), La_2O_3 (Merck, 99%, pre-dried at 900°C for 10 h), ZrO_2(Treibacher, 99,7%), Ta_2O_5 (Treibacher, 99,95%) and Al_2O_3 (Inframat, 99,82%) were used. 10 wt% excess of LiOH was added to compensate for lithium loss during high-temperature treatment. The mixture was thoroughly mixed using an automatic grinder (RM 200, Retsch, Germany) and pressed into pellets before a first calcination step at 850°C for 20 h. The obtained pellets were crushed by a jaw crusher (BB 50, Retsch, Germany) and dry-milled in 250 ml tungsten carbide jars with 20 mm tungsten carbide milling balls at 200 rpm using a planetary ball mill (PM 400, Retsch, Germany) and subsequently sieved with a 50 µm mesh by using a vibratory sieving machine (Analysette 3, Fritsch, Germany). The obtained powder was pressed into pellets and calcined a second time at 1000°C for 20 h. Afterwards, the pellets were crushed and dry-milled again. For use in tape casting, the obtained powder was again ball milled in ethanol with ZrO_2 balls (3 mm) for 60 min at (700 rpm) using a planetary ball mill (Pulverisette 7, Fritsch, Germany). After evaporation of the solvent, the LLZO powder was annealed at 750°C in air for 2 h. The sintering additive Li_3BO_3 was synthesized by solid state synthesis. Stochiometric amounts of H_3BO_3 (Sigma Aldrich, >99.5%) and $LiOH{\cdot}H_2O$ (Applichem, 99%) were homogenized in an agate mortar. The resulting mixture was heated in an Al_2O_3 crucible in air to 650°C with a heating rate of 5 K min^{-1} and a dwell time of 6 h. To reduce the particle size of the commercial $LiNi_{0.82}Co_{0.11}Mn_{0.07}O_2$ (MSE Supplies), the powder was ball milled in isopropanol with 1 mm ZrO_2 balls at 750 rpm for 60 min using a planetary ball mill (Pulverisette 7, Fritsch, Germany) and then dried at 70°C overnight.

4.2 | LLZO Separator Preparation

The starting LLZO:Ta powder was uniaxially pressed into pellets of 13 mm diameter at 120 MPa. The pellets were placed on a MgO plate with a bed of starting powder in a closed Al_2O_3 crucible and sintered at 1175°C for 10 h with heating and cooling rates of 5 K min^{-1}.

4.3 | Composite Cathode Fabrication

Thin composite cathode tapes were prepared by tape casting. First, a polymer solution was prepared beforehand by dissolving (ethylcellulose, Alfa Aesar), the dispersant (BYK 180, Altana), and the additives (PEG 400, Sigma–Aldrich, and Solu Solv, Solutia Inc.) in a solvent mixture of ethanol (VWR, 99.6%) and butanone (VWR, 99.6%) in weight ratios of (7.9:12.7:79). The solution was homogenized on a roller bench for at least 24 h. For NMC-LLZO-LBO tapes, LLZO, NMC, and LBO powders were mixed in a weight ratio of 46:46:8 for NMC-LBO tapes, NMC and LBO were mixed in weight ratios of 92:8. The respective powder mixtures were then added to the polymer solution at a powder-to-solution ratio of 1.8:1 and homogenized using a

planetary mixer (ARE-250, Thinky, Japan) at 1500 rpm for 2 min. The resulting slurries were cast onto Mylar foil using a 450 μm doctor blade and dried at room temperature for at least 4 h. The green tapes were laminated at 300 MPa and 60°C for 2 min, after which 10-mm discs were punched out. The discs were placed on a bed of starting powder on a MgO plate within an Al_2O_3 crucible and sintered in pure oxygen at 750°C for 45 min, with intermediate dwell times of 15 min at 200°C and 600°C. The sintering conditions were empirically optimized by us at the beginning of this study. We attempted to sinter the tapes at the lowest possible temperature (corresponding to the melting point of LBO) and in the shortest possible time to reduce the formation of secondary phases. 750°C is the melting temperature of LBO determined from the TGA measurements. We found that 30 min of sintering at this temperature is not sufficient to obtain mechanically stable layers, but after 45 min, sufficiently stable cathodes could be achieved.

4.4 | Material Characterization

The particle size distribution of the starting and milled powders was checked via laser diffraction (LA950, Horiba Scientific, Japan) with a 650 and a 405 nm laser source, and data were analyzed via the Mie-theory. Phase analysis was performed by powder XRD (D4 Endeavor, Bruker, Germany) with Cu-Kα radiation and a 1D LYNXEYE detector. Le Bail refinements were conducted using Jana2006 software. Thermogravimetric and differential thermal analysis were carried out using a simultaneous thermal analyzer (STA 449C Jupiter, Netzsch, Germany) at a heating rate of $5\,K{\cdot}min^{-1}$ in air from room temperature to 1000°C. Surface topography was examined via chromatic white light interferometry (CT350T, cyberTECHNOLOGIES GmbH, Germany) with P-CHR-10 000 sensor. Raman spectroscopy was performed using a confocal Raman microscope (InVia Qontor, Renishaw, UK) equipped with a 532 nm laser (~2.5 mW) and a $2400\,l{\cdot}mm^{-1}$ grating. Measurements were conducted on powders, the top surface of debinded samples, and polished cross-sections. For powders, spectra from three different spots were averaged. Cross-sections were mapped over $100 \times 40\,\mu m^2$ with a 1 μm step size and 1 s acquisition time with 20 accumulations per point. Top-surface mappings used a 2 μm step size and 10 accumulations per point. All spectra were processed by cosmic-ray removal, normalization, and averaging into representative spectra. Microstructural analysis was performed by scanning electron microscopy (EVO 15, Carl Zeiss Microscopy, Germany) equipped with an energy-dispersive X-ray spectroscopy detector (Ultim Max 100, Oxford Instruments, UK).

4.5 | Cell Assembly and Electrochemical Characterization

To assemble the SSBs, a thin Au current layer (5–15 nm) was deposited onto the composite cathode surface by sputter (108auto Coater, Cressington Scientific Instruments, UK). LLZO pellets of 11.2 mm diameter and 400 μm thickness, prepared as described above, were used as separators. Prior to assembly, the pellets were polished with 4000-grit SiC paper to remove surface impurities and ensure good interfacial contact with the Li metal anodes. Freshly calendared metallic lithium was punch to discs with a diameter of 9 mm and attached to the other side of the LLZO separator by pressing and heating to 300°C. The composite cathode tape and the LLZO separator with a Li-metal anode were connected by using a polymer interlayer. The polymer solution was prepared inside an Ar-filled glovebox by dissolving polycaprolactone grafted cyclodextrin(GCD-PCL) (IMD-4) and LiTFSI (Sigma–Aldrich, >99.5%) in tetrahydrofuran (THF) (Sigma–Aldrich, >99.9%) with a weight ratio of 2:1. For the carbon-containing configurations, 5 wt% of conductive carbon (Alfa Aesar, 99.99%), relative to the polymer mass was first pre-homogenized in THF prior to polymer dissolution to ensure uniform dispersion. A fixed volume of 40 μL of the polymer solution was drop-cast onto the cathode tape on the side not coated with Au, followed by lamination with the LLZO separator. The assembled cells were dried under vacuum at 80°C for 12 h to remove residual solvent.

Electrochemical measurements were performed in a Swagelok cell without external pressure. Prior to testing, the full cells were equilibrated at 60°C for 8 h to homogenize the temperature across all cells and promote good contact between the polymer interlayer and the ceramic components. EIS of the full cells was performed using a potentiostat (VMP-3, BioLogic Sciences Instruments Ltd, France) combined with a climate chamber (VT 4002EMC, Vötsch Industrietechnik VT 4002EMC, Germany). The frequency varied from 3 MHz to 100 mHz with an electrical field perturbation of 10 mV. For fitting and DRT analysis, the Relaxis software (rhd instruments GmbH and Co. KG, Germany) was used. Galvanostatic cycling of the fabricated cells was performed between 3.0 and 4.3 V versus Li/Li^+ with a constant current (cc) density of $40\,\mu A.cm^{-2}$, corresponding to a C-rate of 0.01 C, followed by constant voltage till current dropped to 20 μAcm^{-2}. The GITT experiments were performed using 3 h current pulses ($40\,\mu A{\cdot}cm^{-2}$) followed by 1 h relaxation intervals. At the end of each relaxation step, electrochemical impedance spectra were recorded to monitor the impedance evolution with state of charge and to perform differential resistance analysis (DRT). The Li^+ diffusion coefficients were calculated from the GITT voltage transients using the standard Weppner-Huggins approach.

Author Contributions

Kaouther Touidjine: conceptualization (lead), formal analysis (lead), investigation (lead), visualization (lead), writing – original draft (lead), writing – review and editing (equal). **Christoph Roitzheim**: conceptualization (supporting), formal analysis (equal), investigation (equal), supervision (supporting), writing – original draft (supporting), writing – review and editing (lead). **Xiaochen Liu**: formal analysis (supporting), investigation (equal), validation (equal), writing – original draft (supporting), writing – review and editing (supporting). **Walter Sebastian Scheld**: data curation (equal), formal analysis (supporting), investigation (supporting), supervision (supporting), writing – review and editing (supporting). **Andreas Paulus**: formal analysis (supporting), investigation (supporting), validation (supporting), writing – review and editing (supporting). **Muhammad Zubair**: data curation (supporting), investigation (supporting), validation (supporting), writing – review and editing (supporting). **Mark Huijben**: funding acquisition (equal), resources (supporting), supervision (equal), writing – review and editing (supporting). **Erik Kelder**: funding acquisition (equal), investigation (supporting), resources (supporting), supervision (equal), writing – review and editing (supporting). **Marnix Wagemaker**: funding acquisition (equal), investigation (supporting), resources (supporting),

supervision (equal), writing – review and editing (supporting). **Martin Finsterbusch**: conceptualization (supporting), funding acquisition (equal), investigation (supporting), project administration (equal), supervision (equal), writing original draft (supporting), writing – review and editing (supporting). **Dina Fattakhova-Rohlfing**: conceptualization (equal), funding acquisition (lead), supervision (lead), writing – review and editing (lead).

Acknowledgments

As a part of the DESTINY European doctorate program, the authors acknowledge funding from the European Union's Horizon2020 research and innovation program under the Marie Skłodowska-Curie Actions COFUND-Grant Agreement No: 945357 and the Chairman Prof. Christian Masquelier. The financial support of this work by the German Federal Ministry of Research, Technology, and Space (Bundesministerium für Forschung, Technologie und Raumfahrt, BMFTR), under grant numbers 13XP0434A (FB2-Oxid) and 13XP0432B (FB2-Hybrid) is hereby gratefully acknowledged. The authors thank Helmholtz Institute Münster: Ion conductors for energy storage (IMD-4) for providing the polymer electrolyte used in this study.

Open Access funding enabled and organized by Projekt DEAL.

Funding

This study was supported by BMFTR (13XP0434A (FB2-Oxid), 13XP0432B (FB2-Hybrid)), Destiny (COFUND-Grant Agreement No: 945357).

Conflicts of Interest

The authors declare no conflicts of interest.

Data Availability Statement

The data that support the findings of this study are available in the supplementary material of this article.

References

1. J. Wu, Y. Wang, W. Chen, et al., "Key Challenges and Recent Advances in Advanced Characterization Techniques for LLZO-Based Solid-State Lithium Metal Batteries," *Energy Storage Materials* 82 (2025): 104672.

2. K. V. Kravchyk, D. T. Karabay, and M. V. Kovalenko, "On the Feasibility of All-Solid-State Batteries with LLZO as a Single Electrolyte," *Scientific Reports* 12 (2022).

3. V. Thangadurai, S. Narayanan, and D. Pinzaru, "Garnet-Type Solid-State Fast Li-Ion Conductors for Li Batteries: Critical Review," *Chemical Society Reviews* 43 (2014): 4714–4727.

4. E. Rangasamy, J. Wolfenstine, and J. Sakamoto, "The Role of Al and Li Concentration on the Formation of Cubic Garnet Solid Electrolyte of Nominal Composition Li 7La 3Zr 2O. 12," *Solid State Ionics* 206 (2012): 28–32.

5. L. Buannic, B. Orayech, J. M. L. D. Amo, et al., "Dual Substitution Strategy to Enhance Li+ Ionic Conductivity in Li7La3Zr2O12 Solid Electrolyte," *Chemistry of Materials* 29 (2017): 1769–1778.

6. M. Mann, M. Küpers, G. Häuschen, M. Finsterbusch, D. Fattakhova-Rohlfing, and O. Guillon, "Evaluation of Scalable Synthesis Methods for Aluminum-Substituted li7la3zr2o12 Solid Electrolytes," *Materials* 14 (2021): 6809.

7. C. Schwab, G. Häuschen, M. Mann, et al., "Towards Economic Processing of High-Performance Garnets - Case Study on Zero Li Excess Ga-Substituted LLZO," *Journal of Materials Chemistry A* 11 (2023): 5670–5680.

8. K. V. Kravchyk, M. Klimpel, H. Zhang, and M. V. Kovalenko, *American Chemical Society preprint* (2025).

9. G. T. Hitz, D. W. McOwen, L. Zhang, et al., "High Rate Lithium Cycling in a Scalable Trilayer Li-Garnet-Electrolyte Architecture," *Materials Today* 22 (2019): 50–57.

10. G. V. Alexander, C. Shi, J. O'Neill, and E. D. Wachsman, "Extreme Lithium-Metal Cycling Enabled by a Mixed Ion- and Electron-Conducting Garnet Three-Dimensional Architecture," *Nature Materials* 22 (2023): 1136–1143.

11. B. Hao, W. Chen, J. Wu, Z. J. Jiang, X. Chen, and Z. Jiang, "Long-Term Cycling Stability and Dendrite Suppression in Garnet-Type Solid-State Lithium Batteries via Plasma-Induced Artificial SEI Layer Formation," *Advanced Functional Materials* 35 (2025): 2502429.

12. E. Kurian, J. Pitchai, S. Neelanarayanan, and K. Ramesha, "In Pursuit of All Solid-State Batteries (ASSB): Advances at the Cathode–electrolyte Interface for Garnet-Based ASSB," *RSC Applied Interfaces* 1 (2024): 868–895.

13. M. Rosen, M. Finsterbusch, O. Guillon, and D. Fattakhova-Rohlfing, "Free Standing Dual Phase Cathode Tapes – Scalable Fabrication and Microstructure Optimization of Garnet-Based Ceramic Cathodes," *Journal of Materials Chemistry A* 10 (2022): 2320–2326.

14. C. Roitzheim, Y. J. Sohn, L. Y. Kuo, et al., "All-Solid-State Li Batteries with NCM-Garnet-Based Composite Cathodes: The Impact of NCM Composition on Material Compatibility," *ACS Applied Energy Materials* 5 (2022): 6913–6926.

15. L. Cheng, E. J. Crumlin, W. Chen, et al., "The Origin of High Electrolyte-Electrode Interfacial Resistances in Lithium Cells Containing Garnet Type Solid Electrolytes," *Physical Chemistry Chemical Physics* 16 (2014): 18294–18300.

16. A. Banerjee, X. Wang, C. Fang, E. A. Wu, and Y. S. Meng, *American Chemical Society preprint* (2020).

17. M. M. U. Din, L. Ladenstein, J. Ring, et al., "A Guideline to Mitigate Interfacial Degradation Processes in Solid-State Batteries Caused by Cross Diffusion," *Advanced Functional Materials* 33 (2023): 2303680.

18. M. S. Whittingham, "Lithium Batteries and Cathode Materials," *Chemical Reviews* 104 (2004): 4271–4302.

19. P. Ghorbanzade, A. Pesce, K. Gómez, et al., "Impact of Thermal Treatment on the Li-Ion Transport, Interfacial Properties, and Composite Preparation of LLZO Garnets for Solid-State Electrolytes," *Journal of Materials Chemistry A* 11 (2023): 11675–11683.

20. Z. Huang, K. Liu, L. Chen, Y. Lu, Y. Li, and C. A. Wang, "Sintering Behavior of Garnet-Type Li6.4La3Zr1.4Ta0.6O12 in Li2CO3 Atmosphere and Its Electrochemical Property," *International Journal of Applied Ceramic Technology* 14 (2017): 921–927.

21. A. Bauer, C. Roitzheim, S. Lobe, et al., "Impact of Ni-Mn-Co-Al-Based Cathode Material Composition on the Sintering with Garnet Solid Electrolytes for All-Solid-State Batteries," *Chemistry of Materials* 35 (2023): 8958–8968.

22. Y. Ren, T. Liu, Y. Shen, Y. Lin, and C. W. Nan, "Chemical Compatibility between Garnet-Like Solid State Electrolyte Li6.75La3Zr1.75Ta0.25O12 and Major Commercial Lithium Battery Cathode Materials," *Journal of Materiomics* 2 (2016): 256–264.

23. S. Ohta, S. Komagata, J. Seki, T. Saeki, S. Morishita, and T. Asaoka, "Short Communication All-Solid-State Lithium Ion Battery Using Garnet-Type Oxide and Li3BO3 Solid Electrolytes Fabricated by Screen-Printing," *Journal of Power Sources* 238 (2013): 53–56.

24. R. A. Jonson and P. J. McGinn, "Tape Casting and Sintering of Li7La3Zr1.75Nb0.25Al0.1O12 with Li3BO3 Additions," *Solid State Ionics* 323 (2018): 49–55.

25. K. Tadanaga, R. Takano, T. Ichinose, S. Mori, A. Hayashi, and M. Tatsumisago, "Low Temperature Synthesis of Highly Ion Conductive Li7La 3Zr2O12-Li3BO3 Composites," *Electrochemistry Communications* 33 (2013): 51–54.

26. W. S. Scheld, Y. Collette, K. Touidjine, C. Roitzheim, Y. J. Sohn, and D. Fattakhova-Rohlfing, "Increasing the Cycling Stability of LLZO-Based Solid-State Batteries with Li3BO3 as Catholyte," *Journal of Power Sources* 652 (2025): 237322.

27. W. S. Scheld, *Photonic Sintering of Garnet-Based Solid-State Batteries* (Forschungszentrum Jülich GmbH, 2024).

28. K. Heo, Y. W. Song, D. Hwang, et al., "Effect of a Self-Assembling La2(Ni0.5Li0.5)O4 and Amorphous Garnet-Type Solid Electrolyte Composite on a Layered Cathode Material in All-Solid-State Batteries," *RSC Advances* 12 (2022): 14209–14222.

29. S. Ohta, Y. Kihira, and T. Asaoka, "Spontaneous Formation of a Core–shell Structure by a Lithium Ion Conductive Garnet-Type Oxide Electrolyte for Co-Sintering with the Cathode," *Journal of Materials Chemistry A* 9 (2021): 3353–3359.

30. M. Finsterbusch-Rosen, *Herstellung Von Freitragenden Oxid-Keramischen Batteriekomponenten Für Festkörperbatterien per Folienguss* (University of Duisburg–Essen, 2022).

31. V. Kiyek, C. Schwab, W. S. Scheld, et al., "Direct Precursor Route for the Fabrication of LLZO Composite Cathodes for Solid-State Batteries," *Advanced Science* 11 (2024): 2404682.

32. J. Kim, H. Lee, H. Cha, M. Yoon, M. Park, and J. Cho, "Prospect and Reality of Ni-Rich Cathode for Commercialization," *Advanced Energy Materials* 8 (2018): 1702028.

33. H. J. Noh, S. Youn, C. S. Yoon, and Y. K. Sun, "Comparison of the Structural and Electrochemical Properties of Layered Li[NixCoyMnz]O2 (x = 1/3, 0.5, 0.6, 0.7, 0.8 and 0.85) Cathode Material for Lithium-Ion Batteries," *Journal of Power Sources* 233 (2013): 121–130.

34. K. Touidjine, M. Finsterbusch-Rosen, V. M. Kiyek, et al., "The Impact of Lithium Carbonate on Tape Cast LLZO Battery Separators: A Balanced Interplay between Lithium Loss and Relithiation," *Energy Storage Materials* 71 (2024): 103487.

35. V. Montouillout, H. Fan, L. del Campo, et al., "Ionic Conductivity of Lithium Borate Glasses and Local Structure Probed by High Resolution Solid-Sate NMR," *Journal of Non-Crystalline Solids* 484 (2018): 57–64.

36. C. C. Li and J. H. Jean, "Interactions of Organic Additives with Boric Oxide in Aqueous Barium Titanate Suspensions," *Journal of the American Ceramic Society* 85 (2002): 1441–1448.

37. S. W. Baek, J. M. Lee, T. Y. Kim, M. S. Song, and Y. Park, "Garnet Related Lithium Ion Conductor Processed by Spark Plasma Sintering for All Solid State Batteries," *Journal of Power Sources* 249 (2014): 197–206.

38. H. Zhang, R. Dubey, M. Inniger, et al., "Ultrafast-Sintered Self-Standing LLZO Membranes for High Energy Density Lithium-Garnet Solid-State Batteries," *Cell Reports Physical Science* 4 (2023): 101473.

39. M. Fakhrudin and E. Kartini, In *AIP Conference Proceedings* (American Institute Of Physics Inc., 2022).

40. J. Ji and B. J. Lee, "Analyzing the Effect of Li/Ni Intermixing on Ni-Rich Layered Cathode Structures Using Atomistic Simulation of the Li–Ni–Mn–Co–O Quinary System," *Journal of Power Sources* 556 (2023): 232535.

41. F. Tietz, T. Wegener, M. T. Gerhards, M. Giarola, and G. Mariotto, "Synthesis and Raman Micro-Spectroscopy Investigation of Li7La3Zr2O12," *Solid State Ionics* 230 (2013): 77–82.

42. K. Ben-Kamel, N. Amdouni, A. Mauger, and C. M. Julien, "Study of the Local Structure of LiNi 0.33+δMn 0.33+δCo 0.33-2δO. 2 (0.025 ≤ δ ≤ 0.075) Oxides," *Journal of Alloys and Compounds* 528 (2012): 91–98.

43. C. M. Julien and A. Mauger, AIMS Press preprint (2018).

44. F. Scharf, A. Krude, P. Lennartz, et al., "Synergistic Enhancement of Mechanical and Electrochemical Properties in Grafted Polymer/Oxide Hybrid Electrolytes," *Small* 20 (2024): 2404537.

45. A. Butt, G. Ali, K. T. Kubra, et al., John Wiley and Sons Inc preprint (2022).

46. D. Wang, Q. Sun, J. Luo, et al., "Mitigating the Interfacial Degradation in Cathodes for High-Performance Oxide-Based Solid-State Lithium Batteries," *ACS Applied Materials & Interfaces* 11 (2019): 4954–4961.

47. A. Buchheit, F. Scharf, S. Krämer, M. Grünebaum, M. Winter, and G. Brunklaus, "Enabling High Mass Loadings for Polymer Based All Solid-State Batteries with Temperature Assisted Solvent-Free Vacuum Melt Infiltration," *Energy Storage Materials* 83 (2025): 104670.

48. M. Rosen, R. Ye, M. Mann, et al., "Controlling the Lithium Proton Exchange of LLZO to Enable Reproducible Processing and Performance Optimization," *Journal of Materials Chemistry A* 9 (2021): 4831–4840.

49. M. L. de Souza and M. Morcrette, "Coupling Differential Voltage Analysis and Distribution of Relaxation Times I: Evaluating the Impact of NMC811 Coating in the Degradation of NMC811/Gr Cells," *Journal of Power Sources* 645 (2025): 237184.

50. W. S. Yoon, K. Y. Chung, J. McBreen, and X. Q. Yang, "A Comparative Study on Structural Changes of LiCo1/3Ni1/3Mn1/3O2 and LiNi0.8Co0.15Al0.05O2 during First Charge Using In Situ XRD," *Electrochemistry Communications* 8 (2006): 1257–1262.

51. C. M. Julien, A. Mauger, K. Zaghib, and H. Groult, "Comparative Issues of Cathode Materials for Li-Ion Batteries," *Inorganics* 2 (2014): 132–154.

52. J. Kim, S. Park, S. Hwang, and W. S. Yoon, Korean Electrochemical Society preprint (2022).

53. G. Vardar, W. J. Bowman, Q. Lu, et al., "Structure, Chemistry, and Charge Transfer Resistance of the Interface between Li7La3Zr2O12 Electrolyte and LiCoO2 Cathode," *Chemistry of Materials* 30 (2018): 6259–6276.

Supporting Information

Additional supporting information can be found online in the Supporting Information section.